




Synthesis and investigation of the physical, structural, and radiation shielding properties of the titano-bismuth phosphate glasses

Hicham Es-soufi¹, Leila Ouachou¹, M. I. Sayyed^{2,3,*} , S. Hashim³, Hssain Bih⁴, and Lahcen Bih¹

¹Laboratory of Sciences and Professions of the Engineer, Materials and Processes Department, ENSAM-Meknes Marjane II, Moulay Ismail University, El Mansour, P.O. Box 15290, Meknes, Morocco

²Department of Physics, Faculty of Science, Isra University, Amman, Jordan

³Physics Department, Faculty of Science, Universiti Teknologi Malaysia, 81310 Skudai, Johor, Malaysia

⁴Process Engineering, Computer Science and Mathematics Laboratory (LIPIM), National School of Applied Engineering-Khouribga, Sultan Moulay Slimane University, 23000 Beni Mellal, Morocco

Received: 27 January 2023

Accepted: 16 April 2023

Published online:

25 April 2023

© The Author(s), under exclusive licence to Springer Science+Business Media, LLC, part of Springer Nature 2023

ABSTRACT

The glasses of the $20\text{Li}_2\text{O}-35\text{Li}_2\text{WO}_4-(15-x)\text{TiO}_2-x\text{Bi}_2\text{O}_3-30\text{P}_2\text{O}_5$ system with $0 \leq x \leq 15$ mol% have been prepared using the melt quenching route. X-ray patterns confirmed the amorphous state of the prepared glasses, and the SEM image showed no agglomeration. The structure of these obtained glasses was analyzed by examining the density and molar volume measurements. It was found that the density increased from 3.873 g/cm^3 at LWTBP-0 ($x = 0$ mol%) to 4.740 g/cm^3 at LWTBP-15 ($x = 15$ mol%). But for the molar volume, this is characterized by an increase in molar volume from $39.282 \text{ cm}^3/\text{mol}$ at LWTBP-0 ($x = 0$ mol%) to $44.317 \text{ cm}^3/\text{mol}$ at LWTBP-15 ($x = 15$). Additionally, the oxygen packing density value decreased from 86.554 mol/L (LWTBP-0) to 80.104 mol/L (LWTBP-15), but the oxygen molar volume value increased from $11.553 \text{ cm}^3/\text{mol}$ (LWTBP-0) to $12.484 \text{ cm}^3/\text{mol}$. This is because the amount of Bi_2O_3 in the glassy structure increased from $x = 0$ mol% (LWTBP-0) to $x = 15$ mol% (LWTBP-15). Also, the structure of the prepared glasses has been investigated through infrared spectroscopy, and the band positions and functional groups have been confirmed for the framework phosphates. The radiation shielding properties of the glasses have been analyzed by Phy-X software. The obtained results showed that the maximum mass attenuation coefficient (MAC) values are observable at the energy of 0.284 MeV and are equal to 0.215, 0.247, 0.273, and $0.294 \text{ cm}^2/\text{g}$ for LWTBP-0, LWTBP-5, LWTBP-10, and LWTBP-15, respectively. The sample with the composition $20\text{Li}_2\text{O}-35\text{Li}_2\text{WO}_4-15\text{Bi}_2\text{O}_3-30\text{P}_2\text{O}_5$ has the highest MAC at 0.284 MeV. The half-value layer (HVL) at 0.284 MeV

Address correspondence to E-mail: dr.mabualssayed@gmail.com

decreased from 0.830 to 0.498 cm due to the increase in the Bi_2O_3 content from 0 to 20 mol%.

1 Introduction

Humans can potentially absorb radiation in a variety of settings, including nuclear facilities, medical facilities, research laboratories, nuclear reactors, radiological diagnostics, and other activities. Ionizing radiation with a high energy level can be extremely hazardous to human cells because it can ionize the atoms it comes into contact with by stealing electrons from those atoms. Radiation shields are substances placed between the radiation source and the person or item that has to be shielded to properly harness the advantages of radiation [1–6]. Researchers in the radiation protection sector are particularly interested in developing shields that can absorb gamma photons due to their great penetrating potential. A radiation shield's ability to effectively prevent various types of hazardous radiation should be the defining characteristic of an efficient radiation shield [7, 8]. While there are several materials that can be used for radiation shielding, including concrete, alloys, polymers, and rocks, each material has its own set of advantages and disadvantages. For instance, while concrete is a widely used shielding material due to its low cost and availability, it can produce secondary radiation and has limited effectiveness in blocking high-energy radiation. Similarly, some alloys may provide better shielding performance, but they may be heavier and more expensive than other materials. Polymers are another popular choice due to their flexibility and low weight, but they may not provide sufficient shielding for certain types of radiation. Rocks, on the other hand, can provide natural shielding in some environments, but they may be difficult to work with and require extensive processing. Therefore, it is important to carefully consider the properties of different shielding materials and their potential drawbacks when selecting the most suitable option for a given application [9–12]. Glass has lately received a significant amount of interest because it is transparent to visible light, a characteristic that some other shielding materials do not possess [13–15]. By doping various heavy metal oxides into the glass matrix, it is also possible to dramatically alter the composition of the glass

system. These heavy metal oxides are incorporated into the glass to significantly improve its radiation shielding capabilities and increase its capacity to absorb gamma photons [16]. As an alternative to using concrete as a radiation shielding medium, glasses containing heavy metal oxides may be an appropriate choice. Investigating the structural, optical, physical, and shielding characteristics of possible glasses for the radiation protection industry is therefore crucial research that can enhance the qualities of gamma-ray protecting materials. Phosphate glasses are an attractive type of glass that may be employed for various modern technology purposes, like fabrics and building materials, biomedical applications, shielding materials, and photonic materials [17–19]. Due to their promising features such as high refractive indices, low melting point, low optical dispersions, and high thermal expansion coefficient, phosphate glasses have also undergone extensive research in developing new glasses suitable for the demands of both technology and industry [20, 21].

Additionally, these glasses have been proposed as effective gamma ray shielding materials due to their high dielectric constant, excellent thermal stability, and high density when prepared with a suitable amount of heavy metal oxides [22]. However, very little information is available regarding the phosphate glass employed in the radiation protection applications. The constitution of the original glass should be changed to include heavy metal oxides such as Bi_2O_3 to generate phosphate glasses suitable for use as radiation shielding. There is a possibility that the inclusion of Bi_2O_3 in phosphate glasses will lower the phonon energy; as a result, the radiative characteristics of the glasses may be enhanced [23]. When this fact is taken into account, the glasses under consideration can be considered possible candidates for use in applications involving the shielding of gamma-ray radiation.

Our work showcases a unique approach to the preparation of glasses, as we have developed a novel set of glasses with two transparent and two opaque variants. What sets these glasses apart is their high density, which makes them ideal for use as shielding

materials. The primary objective of our research was to prepare glasses characterized by different techniques and investigate the impact of replacing TiO_2 with Bi_2O_3 on the physical, structural, and shielding properties of a novel $\text{Li}_2\text{O}-\text{Li}_2\text{WO}_4-\text{TiO}_2-\text{Bi}_2\text{O}_3-\text{P}_2\text{O}_5$ glass system. Through our experiments, we were able to identify significant differences in the properties of the glasses with varying levels of Bi_2O_3 . These findings will have important implications for the use of these glasses in various applications, particularly in the field of radiation shielding. Overall, our work represents an important contribution to the field of glass science, and we are excited to see the potential impact that these novel glasses may have in a variety of industries.

2 Experimental protocol

2.1 Sample preparation

The four glasses of the $20\text{Li}_2\text{O}-35\text{Li}_2\text{WO}_4-(15-x)\text{TiO}_2-x\text{Bi}_2\text{O}_3-30\text{P}_2\text{O}_5$ system (with $x = 0-15$ mol%) have been prepared by the melt-quenching route. These glasses are prepared from the raw materials Li_2CO_3 , WO_3 , Bi_2O_3 , TiO_2 , and $\text{NH}_4\text{H}_2\text{PO}_4$, which are purchased from Aldrich (Aldrich, 99%). In the first, the raw materials were weighted according to their stoichiometric coefficients by using an electrical balance and grounded in an agate mortar for around 45 min to obtain a homogeneous mixture. Then, the obtained mixture was placed in an alumina crucible for submission to heat treatments in a programmable electric muffle furnace at 300 °C and 600 °C around 12 h and an hour, respectively, to remove the gases NH_3 , H_2O , and CO_2 . After that, the electrical furnace's temperature was raised to 900 °C and maintained for 30 min, which enabled the transformation of a solid mixture into a liquid mixture. In the end, the melt was quenched on a preheated aluminum plate at a temperature less than the glass transition temperature by 20 °C in order to reduce any remaining thermal stress and prevent the combination from fracturing into small fragments. The obtained glasses were stored in a desiccator to keep them from moisture and labeled as follows: LWTBP-0 ($x = 0$) and LWTBP-5 ($x = 5$) for the transparent glasses; and LWTBP-10 ($x = 10$) and LWTBP-15 ($x = 15$) for the opaque glasses (see Fig. 1).

2.2 Xray diffractometer

The Siemens Diffractometer D5000 with Cu-K radiations (1.5400 Å) at 40 kV and 100 mA, with a scanning angle of 2θ ranging between 10 and 80°, is used for X-ray Diffraction (XRD) analysis. The powder X-ray diffraction patterns (XRD) were determined, and the amorphous properties of prepared glass were studied [24].

2.3 Energy-dispersive X-ray spectroscopy

Energy dispersive X-ray spectroscopy (EDX) is a technique used to identify the elemental composition of a material by analyzing the energy spectrum of X-rays emitted from the sample when it is irradiated with a beam of high-energy electrons. In EDX, a sample is placed in a vacuum chamber and bombarded with a beam of high-energy electrons, which knock inner-shell electrons out of the sample atoms and cause outer-shell electrons to become excited. As the excited electrons return to their ground state, they emit X-rays with unique energies for each element. By measuring the energy and intensity of these X-rays, it is possible to determine the sample's elemental composition [25].

2.4 Scanning electron microscopy (SEM)

Scanning electron microscopy (SEM) is a type of microscopy that uses a beam of high-energy electrons to scan the surface of a sample and create an image of the surface. It is a powerful tool for characterizing the surface morphology and composition of various materials, including metals, semiconductors, ceramics, polymers, and biological specimens. One of the main advantages of SEM is its ability to produce high-resolution images with a high degree of detail. SEM images typically have a resolution of a few nanometers, which is much higher than the resolution of optical microscopes. SEM can also analyze the chemical composition of a sample by using energy-dispersive x-ray spectroscopy (EDS), which measures the energy of the x-rays emitted from the sample when it is irradiated by the electron beam [26].

2.5 Density measurement

A densimeter (H-300S) determined the density measurement for the prepared samples, and water was



Fig. 1 Photo for transparent glasses (LWTBP-0 and LWTBP-5) and opaque glasses (LWTBP-10 and LWTBP-15)

used as a fluid medium. The density value corresponding to each sample is determined from Eq. (1) [27] at room temperature. The average value was calculated after measuring the density of each sample four times to minimize the error of the density measurements, which was at ± 0.03 .

$$d = \frac{m_{\text{air}}}{m_{\text{air}} - m_{\text{water}}} \quad (1)$$

with the terms m_{air} and m_{water} design, respectively, to the sample's weight in air and to the sample's weight in water.

The obtained density values are investigated to calculate the molar volume (V_m) corresponding to each sample, which is calculated from Eq. (2) [27]:

$$V_m = \frac{x_i M_i}{\rho} \quad (2)$$

where (M_i) and (x_i) indicate the sample weight and mole fraction of an oxide component (i) respectively. The error in the calculation of the molar volume was estimated at ± 0.1 .

The density (ρ) was investigated to calculate the oxygen packing density according to Eq. (3) [28]:

$$\text{OPD} = 1000 * C * \left(\frac{\rho}{M}\right) \quad (3)$$

where "C" represents the number of oxygen atoms per formula unit.

As well as the density being used to determine the oxygen molar volume, V_o (Oxygen molar volume (cm^3/mol), can be estimated by Eq. (4) as follows: [29]:

$$V_o = \left(\sum \frac{x_i M_i}{\rho}\right) \left(\frac{1}{\sum x_i n_i}\right) \quad (4)$$

2.6 Infrared spectroscopy

InfraRed analysis was made by an ALPHA Platinum ATR-FTIR spectrometer from Bruker, which was

used for analyzing and recording spectra in the wavenumber range of 1400 cm^{-1} to 400 cm^{-1} , corresponding to the prepared samples. The obtained spectra interpret the structural approach of the framework bands forming the samples.

2.7 Radiation shielding study

The mass attenuation coefficients (MAC) are the percentages of radiation that will be absorbed, scattered, or blocked by a specific layer of shielding material. This notion is the essential factor for many considerable shielding predictions, and it is greatly affected by the composition of the absorber material. In this investigation, we estimated the MAC of the produced glasses using the friendly Phy-X software at different energies between (0.284 and 1.33 MeV) [30].

We can derive the linear attenuation coefficient (LAC) from the MAC. The LAC is a density parameter and can be used to derive other parameters as given in Eqs. (5), (6), and (7) [30]:

$$\text{HVL} = \frac{\ln 2}{\text{LAC}} \quad (5)$$

$$\text{TVL} = \frac{\ln 10}{\text{LAC}} \quad (6)$$

$$\text{MFP} = \frac{1}{\text{LAC}} \quad (7)$$

where the parameters in the previous three equations are the half-value layer, tenth value layer, and mean free path.

Another parameter that could be utilized to characterize the photon shielding competence of these glasses is known as the effective atomic number and can be derived from the following formula

$$Z_{\text{eff}} = \frac{\sum_i w_i A_i \left(\frac{\mu}{\rho}\right)_i}{\sum_i w_i \frac{A_i}{Z_i} \left(\frac{\mu}{\rho}\right)_i} \quad (8)$$

3 Results and discussion

3.1 X-ray diffraction analysis

The XRD patterns of the prepared samples LWTBP-10 and LWTBP-15 are shown in Fig. 2, which display no sharp Bragg's peak but an intense broad diffusion hump around the low-angle region (25–35 (2θ)) and other broad diffusion of low intensity between 40 and 70 (2θ). This clearly indicates an amorphous character or structural disorder within the XRD instrument's resolution limit [31]. When there are no clearly defined planes in the structure on or around which the constituent's atoms are regularly placed, it demonstrates the absence of long-range atomic arrangement and the lack of periodicity of three-dimensional networks [32].

3.2 Energy-dispersive X-ray spectroscopy (EDX)

In our phosphate glasses, EDX is used to determine the relative concentrations of the various elements present in the glass, including phosphorus, oxygen, and any other elements that may be present as impurities. Figure 3 depicts the elemental analysis of the samples LWTBP-10 using the EDX method. The X-ray spectrum produced by the EDX analysis of the sample LWTBP-10 (Fig. 3a) shows the X-rays intensity at various energy levels. Each element (W, T, B,

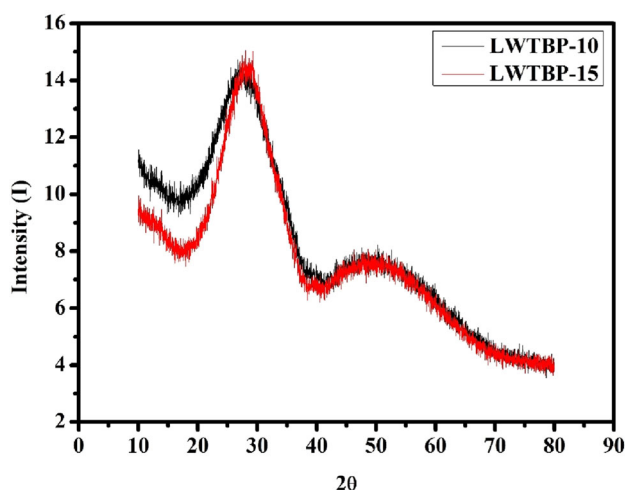


Fig. 2 X-ray diffraction patterns of the samples LWTBP-10 and LWTBP-15

P, and O) has a characteristic set of X-ray lines that are emitted at specific energy levels, and by identifying the lines in the spectrum and measuring their intensities and their distribution map (Fig. 3b). It can be used to determine the relative concentrations of the elements present in the sample LWTBP-0 (see Table 1). EDX analysis of the sample LWTBP-10 can provide us with valuable information about the structure and properties of the glass. For example, the amount of phosphate present in the glass can affect its chemical stability, density, and refractive index. The presence of other elements, such as transition elements, can also affect the glass properties and may be of interest to researchers studying its applications or potential use in various industries. In addition to providing valuable insights into the chemical makeup of phosphate glasses, they can be used to study the effects of different elemental compositions on the glass properties and potential applications (radiation shielding properties) [33, 34].

3.3 Scanning electron microscopy (SEM) analysis

In the case of opaque phosphate glasses, scanning electron microscopy (SEM) is used to study the microstructure of the glass, including the size, shape, and distribution of the glass particles or grains. Furthermore, SEM is applied to study the surface morphology and topography of the glass, as well as any defects present in the material.

Figure 4 shows the surface topographies of the opaque phosphate glasses LWTBP-10 and LWTBP-15 as determined by SEM (a: 2 μm , b: 5 μm , c: 2 μm , d: 5 μm , e: 50 μm). In comparison, the SEM images of the samples LWTBP-10 and LWTBP-15 are characterized by smooth surfaces at 2 μm and 5 μm . Also, the sample LWTBP-15 at 50 μm has a smooth surface without any agglomerations [35, 36]. From the SEM images corresponding to the samples LWTBP-10 and LWTBP-15 and their X-ray diffraction patterns, it can be concluded that these samples (LWTBP-10 and LWTBP-15) have an amorphous nature.

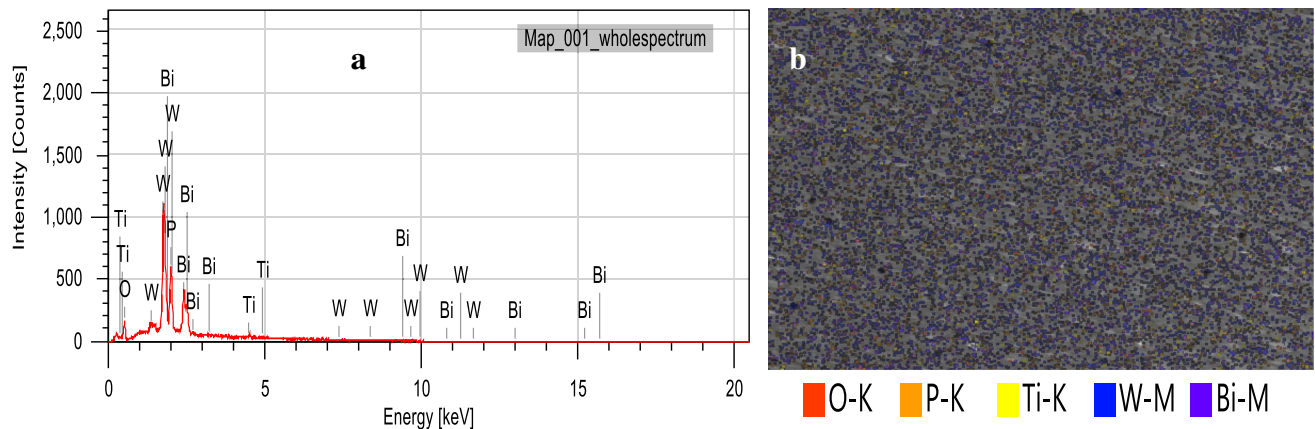


Fig. 3 EDX spectrum **a** and EDX map of sample LWTBP-10 **b**

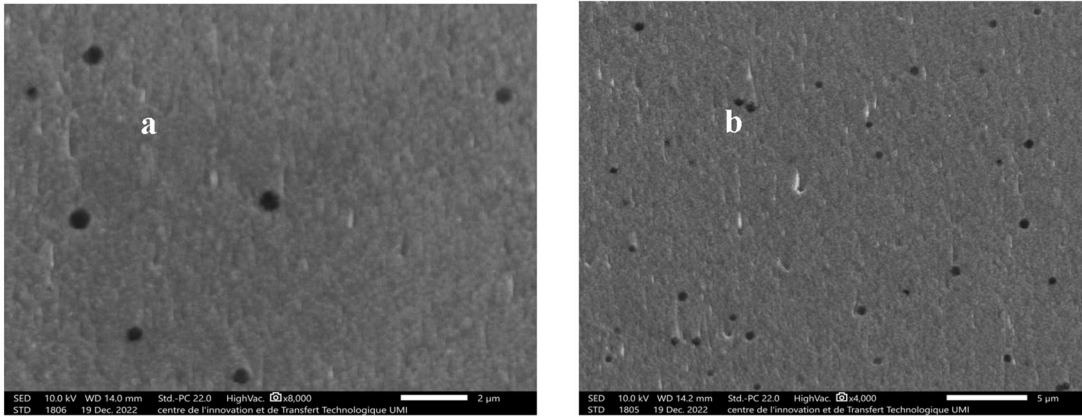
Table 1 EDX elemental analysis of the sample LWTBP-10

Chemical formula	Line	Mass%	Mol%	Cations
O	K			
P ₂ O ₅	K	21.87 ± 0.37	34.32 ± 0.58	4.56
TiO ₂	K	2.50 ± 0.26	6.97 ± 0.74	0.46
WO ₃	M	46.70 ± 0.74	44.87 ± 0.71	2.98
Bi ₂ O ₃	M	28.94 ± 0.60	13.84 ± 0.29	1.84
Total		100.00	100.00	

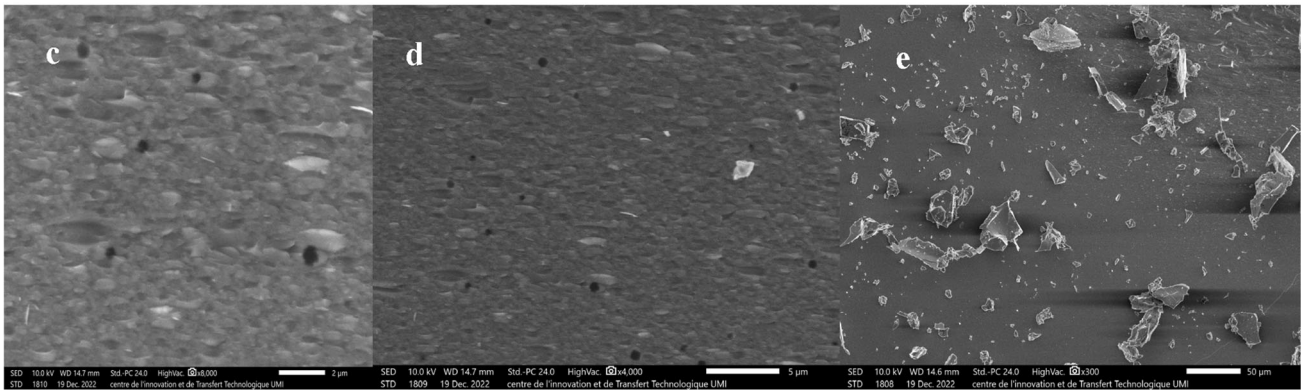
4 Density and molar volume interpretation

Interatomic lengths, atomic radii, molecular weights, compactness, cross-link densities, and interstitial space dimensions are the main determinants of density [32]. In order to analyze the impact of replacing titanium with bismuth on the structural unit alterations in the glassy network, it was chosen to assess the density of the manufactured samples. As a result, the prepared samples densities (volumetric masses, ρ) are measured, and the results are shown in Table 1. The density values (ρ) showed an increase from 3.873 g/cm³ (for the composition LWTBP-0) to 4.740 g/cm³ (for the composition LWTBP-15); see Fig. 5. This increase in density can be associated with the difference in molecular weight between the higher Bi₂O₃ ($M = 465.96 \text{ g}\cdot\text{mol}^{-1}$) and the lower TiO₂ ($M = 79.90 \text{ g}\cdot\text{mol}^{-1}$). The substitution of TiO₂ by Bi₂O₃ made the structure of the samples more compact, and the density increased with the insertion of Bi₂O₃ in the glass network. In addition, an increase in density suggests the creation of structural units with high density, such as BiO₆, in the vitreous network from a structural perspective. A compact or open

structure is formed depending on how the various elements are connected [37]. One must consider the composition dependency of the molar volume to fully comprehend the impact of adding Bi₂O₃ on the glassy structure. As is well known, the molar volume is strongly influenced by interatomic spacing and bond length changes, making it an important parameter for determining the structure's degree of openness. As shown in Table 1, increasing the Bi₂O₃ content increased the molar volume from 39.282 cm³/mol (for the composition LWTBP-0) to 44.317 cm³/mol (for the composition LWTBP-15); see Fig. 5. This behavior could be explained by the fact that titanium oxide (TiO₂) has a smaller molar volume ($V_m = 18.836 \text{ cm}^3/\text{mol}$) than bismuth oxide (Bi₂O₃), which is 52.35 cm³/mol larger. The addition of Bi₂O₃ content increases the opening of the glassy structure by forming nonbridging oxygen (NBO) atoms, which opens up the phosphate network, by lengthening bonds and subsequently interatomic distance [31]. Table 1 shows that substituting Bi₂O₃ for TiO₂ increases the number of oxygen atoms in the structure (from 3.4 ($x = 0$) to 3.55 ($x = 15$), allowing structural units to connect by sharing corners. Interaction between Bi₂O₃ (BiO₆) and P₂O₅ (PO₄) may



Sample LWTBP-10



Sample LWTBP-15

Fig. 4 Surface topographies of opaque phosphate glasses LWTBP-10 (a: 2 μm; b: 5 μm) and LWTBP-15 (c: 2 μm; d: 5 μm; e: 50 μm) obtained from SEM

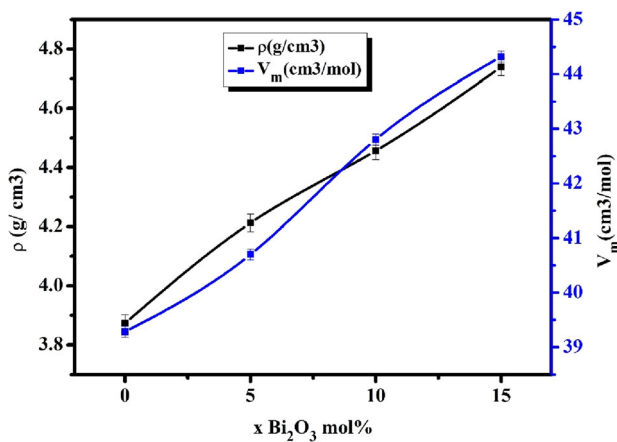


Fig. 5 Variation of the density (g/cm³) and the molar volume (cm³/mol) as a function of the composition (x)

result in the formation of P–O–Bi bonds and increase the connectivity of the polyhedra BiO₆, TiO₆/TiO₄, WO₆/WO₄, and PO₄, which was confirmed by decreasing the oxygen packing density parameter from 86.554 mol/l (for the composition LWTBP-0) to 80.104 mol/l (for the composition LWTBP-15) are associated with the stretching force, which confirmed that the structure could be more compact with the addition of Bi₂O₃ content in the phosphate network [38, 39]. Furthermore, the infrared spectroscopy section will provide proof of this claim. In the meantime, the oxygen packing density is crucial to gauge how tightly the oxide network is packed and to explain how compact the glass structure is [40]. The oxygen packing density has decreased from 86.554 g. L⁻¹ to 80.104 g. L⁻¹ with an increase in Bi₂O₃ content from 0.0 mol% to 15 mol% (see Table 2). The decline in

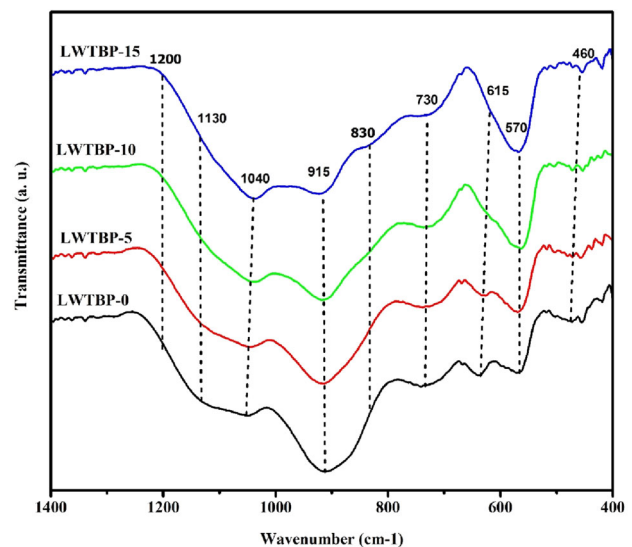
Table 2 Density (ρ) and molar volume of the vitreous samples

Sample Code	x (mol%)	Sample state	Density (g/cm^3)	Molar volume (cm^3/mol)	C(number of oxygens per formula unit)	OPD(Oxygen Packing Density) (mol/l)	V_0 (Oxygen molar volume (cm^3/mol))
LWTBP-0	0	Transparent glass	3.873	39.282	3.4	86.554	11.553
LWTBP-5	5	Transparent-glass	4.212	40.700	3.45	84.766	11.797
LWTBP-10	10	White opaque glass	4.456	42.803	3.5	81.770	12.229
LWTBP-15	15	White opaque glass	4.740	44.317	3.55	80.104	12.484

stiffness, less cross-linked networks [41], which led to an increase in nonbridging oxygen due to the structure of glass having been further extended and being loosely packed [42], may be the cause of the decline in the number of oxygen atoms per unit composition in samples.

4.1 Infrared analysis

The structure of prepared samples of the system $20\text{Li}_2\text{O}-35\text{Li}_2\text{WO}_4-(15-x)\text{TiO}_2-x\text{Bi}_2\text{O}_3-30\text{P}_2\text{O}_5$ (with the codes; LWTBP-0, LWTBP-5, LWTBP-10, and LWTBP-15) was investigated using infrared spectroscopy in the 1400 cm^{-1} to 400 cm^{-1} wavenumber range, and the results are shown in Fig. 6. According to literature [32, 43–50], the bands of the infrared spectra are attributed. Therefore, the principal band positions and their attributions are gathered in Table 3. From Fig. 6, the prominent bands are checked at different positions: 1200 cm^{-1} , 1130 cm^{-1} ,

**Fig. 6** FTIR-ATR spectra corresponding to the glasses LWTBP**Table 3** IR band assignments in the $1400-400\text{ cm}^{-1}$ range frequency for the studied phosphate glasses

Position of band (cm^{-1})	Band assignment
1200	$\nu_{\text{as}}(\text{P}=\text{O})/\nu_{\text{as}}(\text{PO}_2^-)$
1130	$\nu_{\text{s}}(\text{PO}_2^-)$
1040	$\nu_{\text{as}}(\text{PO}_3)^{2-}$
915	$\nu_{\text{as}}(\text{P}-\text{O}-\text{P})/\nu_{\text{as}}(\text{P}-\text{O}-\text{M})$ ($\text{M} = \text{W}$ or Ti)
830	MO_6 ($\text{M} = \text{W}$ or Ti)
730	$\nu_{\text{s}}(\text{P}-\text{O}-\text{P})$
615	$\nu_{\text{s}}(\text{M}-\text{O}-\text{M})$ ($\text{M} = \text{W}$ or Ti)
570	Deformation vibrations of phosphate groups
460	Bi-O bond vibrations of distorted BiO_6 octahedra and deformation modes of $\text{P}-\text{O}^-$ (PO_4) $_3^-$ groups

1040 cm^{-1} , 915 cm^{-1} , 830 cm^{-1} , 730 cm^{-1} , 615 cm^{-1} , 570 cm^{-1} , and 460 cm^{-1} are observed in infrared spectra corresponding to four phosphate samples. Based on previous research [32], we found that the phosphate samples have an asymmetric stretching vibration bond $\text{P}=\text{O}$ ($\nu_{\text{as}}(\text{P}=\text{O})$) due to asymmetric stretching of the $(\text{PO}_2)^-$ mode, $\nu_{\text{as}}(\text{PO}_2^-)$, at 1200 cm^{-1} for the Q^2 units. The broad band, which appears at 1130 cm^{-1} , is associated with the symmetric vibration modes $\nu_s(\text{PO}_2^-)$ of the P-O-P bond of the Q^2 units. The position 1060 cm^{-1} is associated with the bond P-O-P of the mode Q^1 units due to the asymmetric stretching of the $(\text{PO}_3)^{2-}$, $\nu_{\text{as}}(\text{PO}_3)^{2-}$. The band observed at position 935 cm^{-1} is associated with the asymmetric vibration of the bond $\nu_{\text{as}}(\text{P-O-P})$ and/or $\nu_{\text{as}}(\text{P-O-M})$ ($\text{M} = \text{Mo}$ or Ti). The band at position 830 cm^{-1} could be associated with the vibration of the bonds of the polyhedral MO_6 (with $\text{M} = \text{W}$ or Ti). The band observed at 730 cm^{-1} could be attributed to the symmetric vibration of the bond P-O-P. The bands in the low region at position 615 cm^{-1} , are generally assigned as vibration symmetric of the M-O-M (with $\text{M} = \text{W}$ or Ti) bonds. The band located at position 570 cm^{-1} could be attributed to the deformation vibrations of phosphate groups, and the band situated at position 460 cm^{-1} is associated with the deformation modes of P-O^- ($(\text{PO}_4)_3^-$) groups. Infrared spectra, their intensities were normalized to the intensity unit to compare the relative intensities of the peaks, shoulders, and contours. Even after substituting TiO_2 for Bi_2O_3 in the framework, the spectra had changed significantly with an increase in Bi_2O_3 content. Comparing the spectrum of the composition LWTBP-0 ($x = 0$ mol%) with the other compositions $x > 5$, a diminution in two bands at 915 cm^{-1} and 830 cm^{-1} was observed. This diminution may be associated with the formation of the new polyhedra BiO_4 and BiO_6 in place of the polyhedra TiO_4 and TiO_6 [32]. The fact that Bi_2O_3 replaces the decrease in amplitude of the bands around 1200 cm^{-1} as TiO_2 can be explained by considering the decrease in intensity of the vibration band around 1160 cm^{-1} , which is assigned to PO^- vibrations of PO_2^- groups [51]. This is due to non-bridging oxygens involvement in the breakage of $\text{P}=\text{O}$ bonds and the creation of more ionic P-O-Bi and P-O $^-$ bond group terminators. The P-O-P group's asymmetric and symmetric stretching modes are attributed to the vibrational bands near 915 cm^{-1} and 730 cm^{-1} , respectively. As a result, two

P-O-P bridge characteristic bands at 915 cm^{-1} and 730 cm^{-1} simultaneously drop at greater concentrations, indicating that many pyrophosphate units have formed [52]. This band is responsible for the degeneracy of Bi-O bond vibrations in distorted BiO_6 octahedra and the P-O $^-$ ($(\text{PO}_4)_3^-$) group deformation modes [53]. The Bi_2O_3 increase caused the vibrational band at 478 cm^{-1} to become less intense, which shows that a higher concentration is favorable for BiO_6 octahedral units.

4.2 Radiation shielding study

The Phy-X program was used to investigate the radiation shielding properties of the prepared $\text{Li}_2\text{O-Li}_2\text{WO}_4\text{-TiO}_2\text{-P}_2\text{O}_5$ samples between the energies of 0.284 and 1.33 MeV. We figured out the results of our determination of the MAC for the investigated $\text{Li}_2\text{O-Li}_2\text{WO}_4\text{-TiO}_2\text{-P}_2\text{O}_5$ samples in Fig. 7. We could conclude two factors; the energy of the radiation and the various concentrations of Bi_2O_3 on the MAC for the investigated samples. In a practical sense, the MAC value reflects the capacity of the material to absorb radiations for each unit of mass. So, the radiation shielding medium developers aim to develop new materials with a high MAC. In Fig. 7, we chose a sufficiently broad range to enable us to evaluate the shielding capacity of the current samples at both low and moderate energies.

The maximum MAC values are observable at an energy of 0.284 MeV for all of the samples; these values are identical to 0.215, 0.247, 0.273, and 0.294

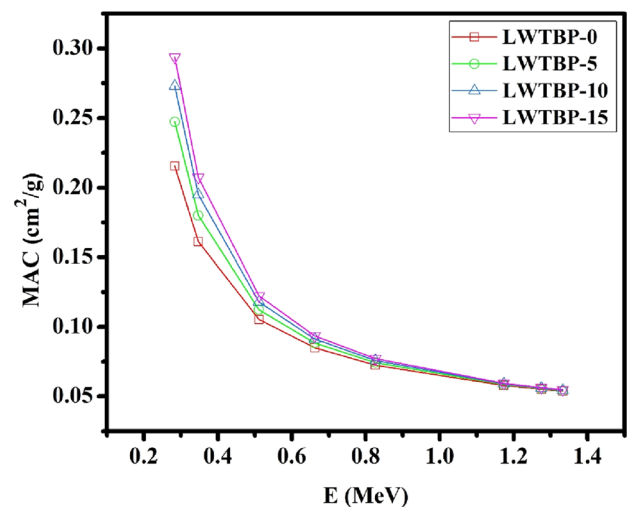


Fig. 7 The mass attenuation coefficient for the $\text{Li}_2\text{O-Li}_2\text{WO}_4\text{-TiO}_2\text{-P}_2\text{O}_5$ glasses with different concentrations of Bi_2O_3

cm^2/g for LWTBP-0, LWTBP-5, LWTBP-10, and LWTBP-15, respectively. A further observation that can be made is that the sample with the composition $20\text{Li}_2\text{O}-35\text{Li}_2\text{WO}_4-15\text{Bi}_2\text{O}_3-30\text{P}_2\text{O}_5$ which has the highest concentration of Bi_2O_3 , has the highest MAC at this energy, whereas the sample with the composition $20\text{Li}_2\text{O}-35\text{Li}_2\text{WO}_4-15\text{TiO}_2-30\text{P}_2\text{O}_5$, which does not contain any Bi_2O_3 , has the lowest MAC. At this level, the other energies have been examined and tested. The results shown in Fig. 7 revealed that after 0.511 MeV, the MAC begins declining at a slower rate than before. This is due to the domination of the Compton scattering for the last energies. From the MAC results, the prepared samples become less efficient at absorbing the high-energy gamma rays because these radiations have a strong ability to penetrate across the samples. For higher energies, 1.33 MeV for example, the MAC for the four prepared samples has almost the same MAC of $0.054 \text{ cm}^2/\text{g}$. We can summarize the findings from the MAC: the samples with high Bi_2O_3 are better shields, and the samples are more effective in shielding the radiations with low energy.

We compared the linear attenuation coefficient (LAC) for our newly developed glasses with three glasses (Fig. 8). The details of these three glasses are given in Ref. [54]. From the figure, LWTBP-0 and RS-360 have almost the same LAC at 0.662 MeV, LWTBP-5, LWTBP-10, and LWTBP-15 have better

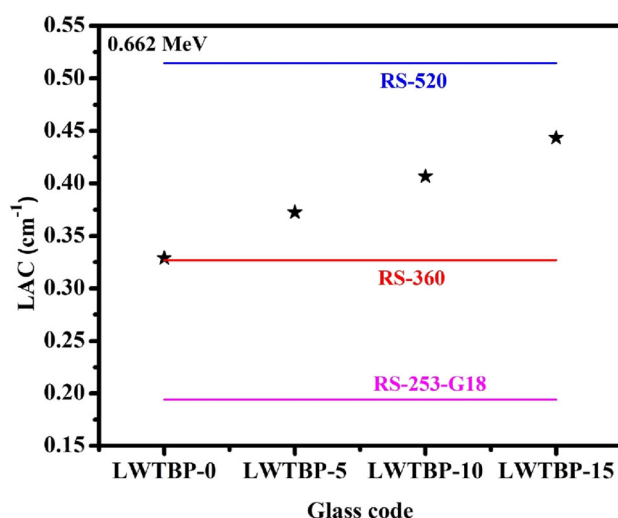


Fig. 8 The linear attenuation coefficient for the $\text{Li}_2\text{O}-\text{Li}_2\text{WO}_4-\text{TiO}_2-\text{P}_2\text{O}_5$ glasses with different concentrations of Bi_2O_3 in comparison with other glasses at 0.662 MeV

attenuation performance than RS-253-G18, while our glasses have a lower LAC than RS-520.

We analyzed the half-value layer (HVL) for the prepared $\text{Li}_2\text{O}-\text{Li}_2\text{WO}_4-\text{TiO}_2-\text{P}_2\text{O}_5$ glasses with four concentrations of Bi_2O_3 as a function of the energy in Fig. 9. The HVL exhibited a trend in the opposite direction to the Bi_2O_3 concentration; specifically, the HVL decreased as the Bi_2O_3 concentration increased. For instance, elevating the total amount of Bi_2O_3 from 0 to 20 mol% leads to a reduction in the HVL from 0.830 to 0.498 cm (this is at 0.284 MeV). The increment of Bi_2O_3 content from 0 to 20 mol% causes the HVL to decline from 1.111 to 0.705 cm when the energy level is 0.347 MeV. Moreover, due to the presence of Bi_2O_3 , the HVL at 0.511 MeV decreases from 1.698 to 1.195 cm. The density of the produced glasses is connected to the reported downward trend in the HVL brought about by adding Bi_2O_3 . It is widely known that the HVL may be calculated using the fundamental expression $\text{HVL} = \ln^2 / (\text{density} \times \text{LAC})$, Therefore, the HVL is negatively correlated to the density of the medium.

From Table 2, the density increased from 3.8732 to $4.7398 \text{ g}/\text{cm}^3$ due to the incorporation of Bi_2O_3 , leading to a reduction in HVL. This outcome fits well with other results that have been reported for glasses and other materials [7, 8, 55].

We analyzed the radiation shielding features for the prepared $\text{Li}_2\text{O}-\text{Li}_2\text{WO}_4-\text{TiO}_2-\text{P}_2\text{O}_5$ glasses with four concentrations of Bi_2O_3 in terms of the effective atomic number, Z_{eff} (Fig. 10). The Z_{eff} increases when

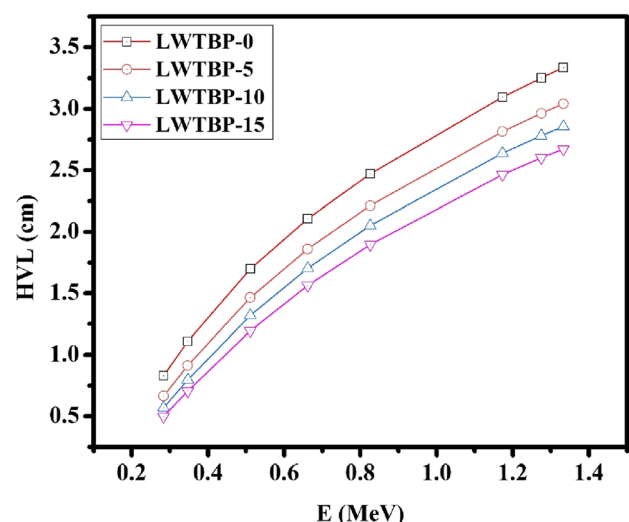


Fig. 9 The half-value layer for the $\text{Li}_2\text{O}-\text{Li}_2\text{WO}_4-\text{TiO}_2-\text{P}_2\text{O}_5$ glasses with different concentrations of Bi_2O_3

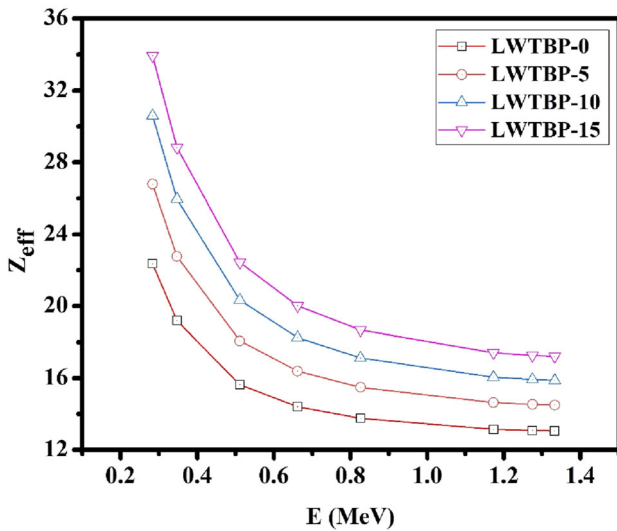


Fig. 10 The effective atomic number for the $\text{Li}_2\text{O-Li}_2\text{WO}_4\text{-TiO}_2\text{-P}_2\text{O}_5$ glasses with different concentrations of Bi_2O_3

the concentration of Bi_2O_3 increases from 0 to 15 mol%. The free Bi_2O_3 sample (LWTBP-0), the Z_{eff} at 0.284 MeV is 22.36, while with the inclusion of 5, 10 and 15 mol% of Bi_2O_3 , the Z_{eff} values increase to 26.78, 30.60 and 33.92 respectively. At the same concentrations of Bi_2O_3 (5, 10 and 15%) at 0.347 MeV, the Z_{eff} increases from 19.18 for the free- Bi_2O_3 , to 22.76, 25.95 and 28.81 with 5, 10 and 15 mol% respectively. There is a correlation between the amount of Bi_2O_3 and TiO_2 in the glasses and the increase found in the Z_{eff} . As we moved from LWTBP-0 to LWTBP-15, the Bi_2O_3 content increased from 0 to 15 mol% at the expense of TiO_2 .

Therefore, the sample LWTBP-15 has the highest concentration of Bi_2O_3 . It is widely known that the atomic numbers of Bi and Ti are 83 and 22, which helps to explain why LWTBP-15 has been found to have the highest Z_{eff} . On the other hand, for a particular composition, the Z_{eff} also heavily depends on the energy of the radiation. For illustration, for the glass with a composition of $20\text{Li}_2\text{O-35Li}_2\text{WO}_4\text{-15TiO}_2\text{-30P}_2\text{O}_5$, the Z_{eff} starts at a high value of 0.284 MeV (i.e. 22.36), then sharply decreases and reaches to 14.40 at 0.662 MeV, and then still decreases to 13.08 and 13.05 at 1.275 and 1.333 MeV. The same trend is observed for the rest of compositions. For example, the Z_{eff} values at the previous energies for the sample containing 5 mol% of Bi_2O_3 are 26.78, 16.39, 14.54 and 14.50.

We determined the MFP for the $\text{Li}_2\text{O-Li}_2\text{WO}_4\text{-TiO}_2\text{-P}_2\text{O}_5$ glasses with four concentrations of Bi_2O_3

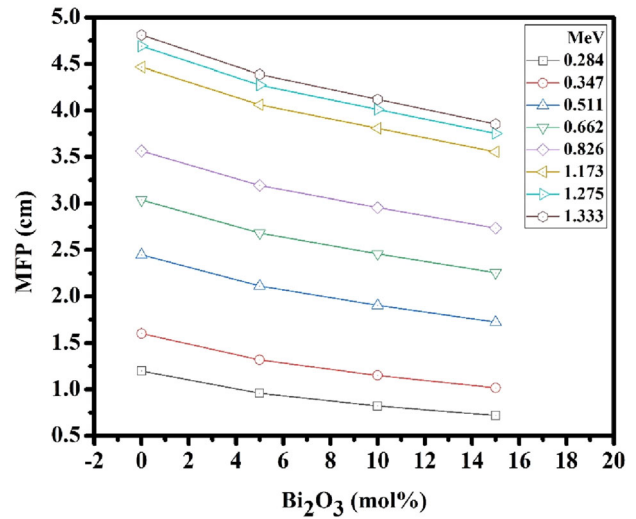


Fig. 11 The mean free path for the $\text{Li}_2\text{O-Li}_2\text{WO}_4\text{-TiO}_2\text{-P}_2\text{O}_5$ glasses with different concentrations of Bi_2O_3

and Fig. 11 shows the results plotted as a function of Bi_2O_3 at the tested energies. The Bi_2O_3 level and MFP relationship showed a similar trend as the HVL. This observable regularity may be traced back to the fact that both MFP and HVL are generated using the LAC values as their starting point.

The MFP decreases when Bi_2O_3 is added, and this effect is seen at any of the chosen energies. This demonstrates how important it is to add the Bi_2O_3 to reduce the specimen's thickness required for radiological protection. The inclusion of Bi_2O_3 results in a decrease in the MFP from 1.198 to 0.719 cm when the energy level is 0.284 MeV. Moreover, the MFP at 0.347 MeV decreases from 1.602 cm (for LWTBP-0) to 1.017 cm (for LWTBP-15). At a high energy level (1.275 MeV), the MFP for the aforementioned samples is respectively 4.692 and 3.752 cm. This suggests the thickness of the specimen, which can lower the intensity as the photons energy increases. Previous research has shown that high energy correlates with the necessity for a thicker specimen to reduce the intensity of the photons because higher energy radiation has a greater chance of entering the material [56–58]. Therefore, we noticed that the MFP is achieved at about 3.8–4.8 cm for an energy of 1.333 MeV.

Figure 12 illustrates how the TVL is affected by various Bi_2O_3 concentrations. The addition of Bi_2O_3 is correlated with a downward trend in the TVL across the board for all energy levels. In addition to this, the TVL demonstrates an upward trend. This is the same

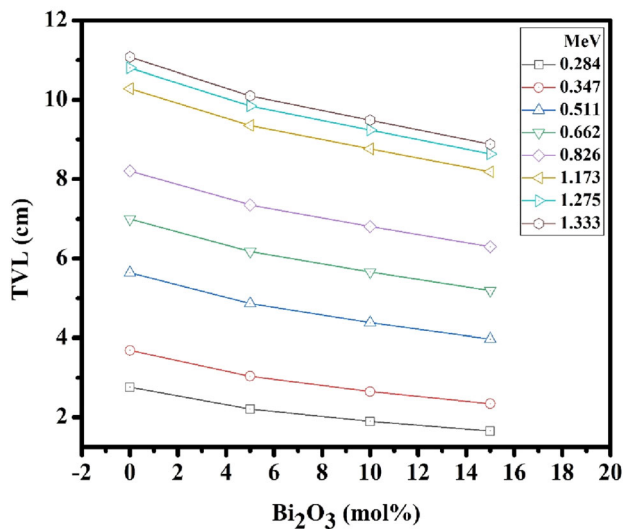


Fig. 12 The tenth value layer for the $\text{Li}_2\text{O}-\text{Li}_2\text{WO}_4-\text{TiO}_2-\text{P}_2\text{O}_5$ glasses with different concentrations of Bi_2O_3

result obtained from HVL data. The maximum TVL is reported at 1.333 MeV (8.878 cm for LWTBP-15 and 11.079 cm for LWTBP-0). The Bi_2O_3 has a notable impact on the TVL, and the sample with lower Bi_2O_3 content has a higher TVL than the sample with high Bi_2O_3 content. So, one effective way to reduce the dimension of the shielding glasses is to increase the concentrations of Bi_2O_3 .

We compared the TVL for our glasses with three commercial glasses that are widely used for radiation shielding applications. The comparison was done at one energy, specifically 0.511 MeV (see Fig. 13). The

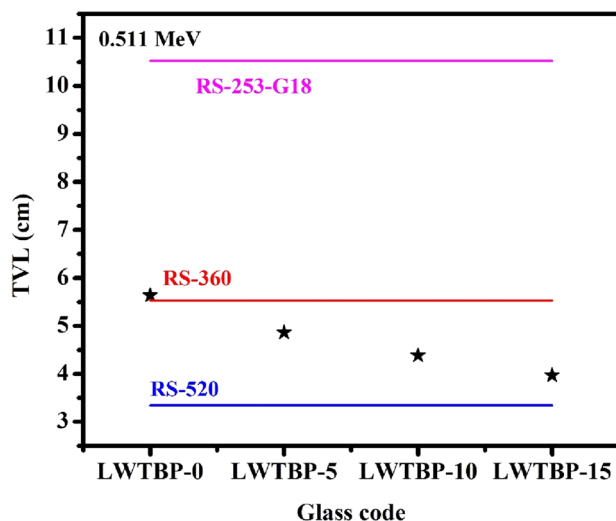


Fig. 13 comparison between the tenth value layer of our glasses with other commercial glasses at 0.511 MeV

TVL values for our glasses LWTBP-0, LWTBP-5, LWTBP-10 and LWTBP-15 were found to be 5.64, 4.87, 4.38, and 3.97 cm, respectively. Among our glasses, LWTBP-0 had the highest TVL value, while LWTBP-15 had the lowest. Compared to the commercial glasses, RS-253-G18 had the highest TVL value of 10.52 cm, followed by RS-360 at 5.53 cm. Our glass LWTBP-0 had a similar TVL value to RS-360 of 5.64 cm, followed by LWTBP-10 at 4.38 cm, LWTBP-5 at 4.87 cm, and LWTBP-15 at 3.97 cm. RS-520 had the lowest TVL value among all the glasses of 3.34 cm. It should be noted that the TVL values for the glasses can vary depending on the energy of the incident radiation, and therefore, the comparison is limited to 0.511 MeV radiation.

5 Conclusion

The phosphate glasses $20\text{Li}_2\text{O}-35\text{Li}_2\text{WO}_4-(15-x)\text{TiO}_2-x\text{Bi}_2\text{O}_3-30\text{P}_2\text{O}_5$ with $0 \leq x \leq 15$ mol% were synthesized in this study using the melt-quenching technique. These samples' amorphous state, as determined by X-ray diffraction and confirmed by SEM images, revealed no agglomeration on the surface of the analyzed samples. The glasses density and molar volume are increased from 3.873 g/cm^3 to 4.740 g/cm^3 and from $39.282 \text{ cm}^3/\text{mol}$ (LWTBP-0) to $44.317 \text{ cm}^3/\text{mol}$ (LWTBP-15), respectively, with increasing Bi_2O_3 content in the glass framework. In addition, by increasing the amount of Bi_2O_3 in the glassy structural from $x = 0$ mol% (LWTBP-0) to $x = 15$ mol% (LWTBP-15), the oxygen packing density value decreased from 86.554 mol/L (LWTBP-0) to 80.104 mol/L (LWTBP-15), but the oxygen molar volume value increased from $11.553 \text{ cm}^3/\text{mol}$ (LWTBP-0) to $12.484 \text{ cm}^3/\text{mol}$ (LWTBP-15). While adding Bi_2O_3 into the glassy network increased the nonbridging oxygens (NBO), as confirmed from the structure analysis by infrared spectroscopy. The radiation shielding factors for the present glasses are reported in this study using the Phy-X software. The maximum MAC values are observable at an energy of 0.284 MeV for all samples; these values are identical to 0.215, 0.247, 0.273, and $0.294 \text{ cm}^2/\text{g}$ for LWTBP-0, LWTBP-5, LWTBP-10, and LWTBP-15, respectively. The sample with the composition $20\text{Li}_2\text{O}-35\text{Li}_2\text{WO}_4-15\text{Bi}_2\text{O}_3-30\text{P}_2\text{O}_5$ which has the highest concentration of Bi_2O_3 , has the highest MAC. The inclusion of Bi_2O_3 results in a decrease in the

MFP from 1.198 to 0.719 cm when the energy level is 0.284 MeV. The MFP at 0.347 MeV decreases from 1.602 cm (for LWTBP-0) to 1.017 cm (for LWTBP-15). These MFP results suggested that the thickness of the specimen can lower the photon intensity as the energy increases.

Acknowledgements

M.I.Sayyed and S.Hashim gratefully acknowledge Universiti Teknologi Malaysia for providing Prominent Visiting Researcher Scheme (RJ3000.7113.3F000) initiatives under the Department Deputy of Vice-Chancellor (Research and Innovation).

Author contributions

HE—Writing original draft, writing, editing and proof reading; LO—visualization; MIS—Writing original draft, writing, editing and proof reading; SH—proof reading; HB—Visualization; LB—Supervision.

Funding

The authors have not disclosed any funding

Data availability

The datasets generated during and/or analyzed during the current study are available from the corresponding author on reasonable request.

Declarations

Conflict of interest The authors declare that they have no known conflicts of interest.

References

- X. Huang, J. Li, X. Liu, G. Zhang, Radiation shielding materials for nuclear facilities: a review. *Prog. Nucl. Energy* **139**, 103883 (2022)
- M. Dong, S. Zhou, X. Xue, M.I. Sayyed, D. Tishkevich, A. Trukhanov, C. Wang, Study of comprehensive shielding behaviors of chambersite deposit for neutron and gamma ray. *Prog. in Nucl. ener.* **146**, 104155 (2022)
- R. Jafari, E. Rezaee, E. Zarifi, Design of a gamma ray shielding in the waste management plant of Bushehr nuclear power plant. *J. Radiol. Prot.* **42**, 238–248 (2022)
- M. Dong, X. Xue, H. Yang, D. Liu, C. Wang, Z. Li, A novel comprehensive utilization of vanadium slag: As gamma ray shielding material. *J. Hazard. Mater.* **318**, 751–757 (2016)
- X. Zhang, C. Liu, X. Zhang, H. Yang, X. Wang, Optimization of radiation shielding thickness for computed tomography using Monte Carlo simulation. *Radiat. Prot. Dosim.* **199**, 82–87 (2022)
- F.I. El-Agawany, O.L. Tashlykov, K.A. Mahmoud, Y.S. Rammah, The radiation-shielding properties of ternary SiO₂–SnO–SnF₂ glasses: simulation and theoretical study. *Cer. Inter.* **46**(15), 23369–23378 (2020)
- I.S. Mahmoud, S.A. Issa, Y.B. Saddeek, H.O. Tekin, O. Kilicoglu, T. Alharbi, R. Elsaman, Gamma, neutron shielding and mechanical parameters for lead vanadate glasses. *Cer. Inter.* **45**(11), 14058–14072 (2019)
- M.I. Sayyed, I.A. El-Mesady, A.S. Abouhaswa, A. Askin, Y.S. Rammah, Comprehensive study on the structural, optical, physical and gamma photon shielding features of B₂O₃–Bi₂O₃–PbO–TiO₂ glasses using WinXCOM and Geant4 code. *J. Mol. Str.* **1197**, 656–665 (2019)
- M.F. Ahmad, N.A. Hanif, Assessment of gamma-ray shielding properties of concrete containing different types of aggregates. *J. Env. Rad.* **231–232**, 106433 (2021)
- B.F. Debnath, S.K. Basu, A.K. Chakraborty, S.K. Saha, S.K. Sahoo, Shielding properties of different grades of high-density concrete for high energy gamma-rays and neutrons. *Radiat. Phys. Chem.* **188**, 109596 (2021)
- H.M. Ahmed, A.E. Fathy, A.A. El-Desoky, A.S.A. Selim, Investigation of the shielding efficiency of some natural and artificial stones against cosmic radiation. *Results in Physics* **26**, 104613 (2022)
- M. Yousaf, W.A. Khan, A. Raza, G. Murtaza, M. Arif, T. Hussain, Comparative study of radiation shielding properties of polymeric materials. *Radiat. Eff. Defects Solids* **177**, 41–51 (2022)
- M. Ismail, S.K. Ghoshal, M.A. Abd El-Latif, S.S. El-Dek, A. El-Tayeb, Radiation shielding properties of bismuth-titanate glasses containing magnesium. *J. Non-Crys. Sol.* **562**, 120699 (2021)
- Q. Li, J. Li, J. Tang, Y. Li, X. Li, Study of the radiation shielding properties of bismuth-titanium-phosphate glass using Geant4 simulation. *Radiat. Phys. Chem.* **189**, 1–7 (2022)
- A. Kumar, D.K. Gaikwad, S.S. Obaid, H.O. Tekin, O. Agar, M.I. Sayyed, Experimental studies and Monte Carlo

- simulations on gamma ray shielding competence of $(30+x)$ $\text{PbO}_{10}\text{WO}_3-10\text{Na}_2\text{O}-10\text{MgO}-(40-x)\text{B}_2\text{O}_3$ glasses. *Prog. in Nucl. Ener.* **119**, 103047 (2020)
16. M.T. Zidan, A.M. Ahmed, S.S. Abdel-Rahman, A.M. El-Khayatt, Gamma-ray shielding and mechanical properties of novel bismuth oxide-titanium oxide-phosphate glass-ceramics. *J. Non-Crys. Sol.* **627**, 119346 (2022)
 17. J.C. Knowles, Phosphate based glasses for biomedical applications. *J. Mat. Chem.* **13**(10), 2395–2401 (2003)
 18. S. Kaewjaeng, N. Chanthima, J. Thongdang, S. Reungsri, S. Kothan, J. Kaewkhao, Synthesis and radiation properties of $\text{Li}_2\text{O}-\text{BaO}-\text{Bi}_2\text{O}_3-\text{P}_2\text{O}_5$ glasses. *Mat. Tod. Proc.* **43**, 2544–2553 (2021)
 19. K.A. Matori, M.I. Sayyed, H.A.A. Sidek, M.H.M. Zaid, V.P. Singh, Comprehensive study on physical, elastic and shielding properties of lead zinc phosphate glasses. *J. Non-Cryst. Sol.* **457**, 97–103 (2017)
 20. K. Amin Matori, M.H. Mohd Zaid, H.J. Quah, S.H. Abdul Aziz, Z. Abdul Wahab, M.S. Mohd Ghazali, Studying the effect of ZnO on physical and elastic properties of $(\text{ZnO})_x(\text{P}_2\text{O}_5)_{1-x}$ glasses using nondestructive ultrasonic method. *Adv. Mat. Sci. Eng.* (2015). <https://doi.org/10.1155/2015/596361>
 21. V. Zanganeh, Effect of WO_3 addition on mechanical, structural, optical, and radiation shielding properties of lead boro phosphate glasses system using Monte Carlo simulation. *Opt.* **269**, 169900 (2022)
 22. C.S. Sarumaha, J. Rajagukguk, J. Tongdang, N. Chanthima, H.J. Kim, S. Kothan, J. Kaewkhao, Effect of Gd_2O_3 in $\text{Li}_2\text{O}-\text{AlF}_3-\text{CaF}_2-\text{P}_2\text{O}_5-\text{Eu}_2\text{O}_3$ glasses for laser medium and X-rays detection material applications. *Rad. Phy. and Chem.* **199**, 110362 (2022)
 23. M.A. Marzouk, F.H. ElBatal, UV-visible and infrared absorption spectra of Bi_2O_3 in lithium phosphate glasses and effect of gamma irradiation. *Appl. Phys. A* **115**(3), 903–912 (2014)
 24. S. Mayr, C. Randau, W. Kreuzpaintner, Automatic attenuator upgrade for a Siemens D500 diffractometer via a generic software library to overcome hardware limitations. *Nucl. Instr. Meth. Phys. Res. Accel. Spect. Detec. Ass. Equ.* **855**, 61–64 (2017)
 25. Z.S. Duma, T. Sihvonen, J. Havukainen, V. Reinikainen, S.P. Reinikainen, Optimizing energy dispersive X-Ray Spectroscopy (EDS) image fusion to Scanning Electron Microscopy (SEM) images. *Mic.* **163**, 103361 (2022)
 26. S.S. Bangaru, C. Wang, X. Zhou, M. Hassan, Scanning electron microscopy (SEM) image segmentation for microstructure analysis of concrete using U-net convolutional neural network. *Aut. in Const.* **144**, 104602 (2022)
 27. H. Es-soufi, H. Bih, M.I. Sayyed, L. Bih, Impact of TiO_2 on physical, optical, and radiation shielding properties of tungsten-based glasses. *Opt.* **170**, 400 (2022)
 28. G. Upender, M. Prasad, Vibrational, Optical and EPR studies of $\text{TeO}_2-\text{Nb}_2\text{O}_5-\text{Al}_2\text{O}_3-\text{V}_2\text{O}_5$ glass system doped with vanadium. *Opt.* **127**(22), 10716–10726 (2016)
 29. M.M. Elokr, Y.M. AbouDeif, Optical, elastic properties and DTA of TNZP host tellurite glasses doped with Er^{3+} ions. *J. Mol. Str.* **1108**, 257–262 (2016)
 30. M.A. Imheidat, M.K. Hamad, M.I. Sayyed, Y.S.M. Alajerami, N.S. Prabhu, S.D. Kamath, M.H.A. Mhareb, Correlation between mechanical, gamma shielding features and tellurium oxide concentrations in molybdenum aluminum strontium borate glass. *Opt.* **272**, 170336 (2023)
 31. E. Şakar, Ö.F. Özpolat, B. Alım, M.I. Sayyed, M. Kurudirek, Phy-X/PSD: development of a user friendly online software for calculation of parameters relevant to radiation shielding and dosimetry. *Rad. Phy. and Chem.* **166**, 108496 (2020)
 32. H. Es-soufi, L. Bih, Synthesis, Characterization, and Optical Properties of Titano-Molybdenum Phosphate Glasses. *J. Elec. Mat.* **51**(5), 2528–2544 (2022)
 33. H. Es-Soufi, L. Bih, B. Manoun, P. Lazor, Structure, thermal analysis and optical properties of lithium tungsten-titanophosphate glasses. *J. Non-Cry. Sol.* **463**, 12–18 (2017)
 34. U. Kara, G. Susoy, S.A. Issa, W. Elshami, N.Y. Yorgun, M.M. Abuzaid, H.O. Tekin, Scanning electron microscopy (SEM), energy-dispersive X-ray (EDX) spectroscopy and nuclear radiation shielding properties of $[\alpha\text{-Fe}^{3+} \text{O}(\text{OH})]$ -doped lithium borate glasses. *App. Phys. A* **126**(7), 1–14 (2020)
 35. S.K. Barik, A. Senapati, S. Balakrishnan, K. Ananthasivan, Synthesis and characterization of rare-earth doped aluminium phosphate glasses. *Prog. in Nucl. Ene.* **152**, 104372 (2022)
 36. N.R.K. Chand, B.K. Sudhakar, G. Ravikumar, V. Gayathri, P. Devika, T. Vennela, C.S. Rao, Influence of multi valent states of vanadium ions in ZnO doped novel calcium fluoro phosphate bio glasses. *J. Mech. Beh. of Bio. Mat.* **105**, 230 (2022)
 37. F. Wang, Y. Wang, D. Zhang, Y. Hao, Q. Liao, H. Zhu, Y. Zhu, Effects of MoO_3 and Nd_2O_3 on the structural features, thermal stability and properties of iron-boron-phosphate based glasses and composites. *J. Nucl. Mat.* **560**, 153500 (2022)
 38. A. Shaim, M. Et-Tabirou, L. Montagne, G. Palavit, Role of bismuth and titanium in $\text{Na}_2\text{O}-\text{Bi}_2\text{O}_3-\text{TiO}_2-\text{P}_2\text{O}_5$ glasses and a model of structural units. *Mater. Res. Bull.* **37**(15), 2459–2466 (2002)
 39. S. Bale, S. Rahman, Spectroscopic and physical properties of $\text{Bi}_2\text{O}_3-\text{B}_2\text{O}_3-\text{ZnO}-\text{Li}_2\text{O}$ glasses. *Int. Sch. Res. Not.* (2012). <https://doi.org/10.5402/2012/634571>
 40. N. Elkhoshkhany, S. Marzouk, M. El-Sherbiny, H. Ibrahim, B. Burtan-Gwizdala, M.S. Alqahtani, E.S. Yousef,

- Investigation of structural, physical, and attenuation parameters of glass: $\text{TeO}_2\text{-Bi}_2\text{O}_3\text{-B}_2\text{O}_3\text{-TiO}_2\text{-RE}_2\text{O}_3$ (RE: La, Ce, Sm, Er, and Yb), and applications thereof. *Materials* **15**(15), 5393 (2022)
41. M. Farouk, A. Samir, F. Metawe, M. Elokr, Optical absorption and structural studies of bismuth borate glasses containing Er^{3+} ions. *J. Non-Cry. Sol.* **371–372**, 14–21 (2013)
 42. M. Çelikbilek, A. Erçin Ersundu, S. Aydin, Glass formation and characterization studies in the $\text{TeO}_2\text{-WO}_3\text{-Na}_2\text{O}$ system. *J. Amer. Cer. Soc.* **96**(5), 1470–1476 (2013)
 43. M. Altaf, M.A. Chaudhry, Physical properties of lithium containing cadmium phosphate glasses. *J. Mod. Phys* **1**, 201–205 (2010)
 44. R.K. Brow, The structure of simple phosphate glasses. *J. Non-Cry. Sol.* **263**, 1–28 (2000)
 45. M. Mariyappan, K. Marimuthu, M.I. Sayyed, M.G. Dong, U. Kara, Effect Bi_2O_3 on the physical, structural and radiation shielding properties of Er^{3+} ions doped bismuth sodiumfluoroborate glasses. *J. Non-Cry. Sol.* **499**, 75–85 (2018)
 46. Y.H. Na, N.J. Kim, S.H. Im, J.M. Cha, B.K. Ryu, Effect of Bi_2O_3 on structure and properties of zinc bismuth phosphate glass. *J. Cer. Soc. of Japan* **117**(1371), 1273–1276 (2009)
 47. S. Damodaraiah, V.R. Prasad, Y.C. Ratnakaram, Impact of Bi_2O_3 on structural properties and lasing effects in Nd^{3+} doped bismuth phosphate glasses at 1.053 μm emission. *Spect. Acta. Mol. Bio. Spec.* **181**, 264–269 (2017)
 48. P.S. Rao, C. Rajyasree, A.R. Babu, P.V. Teja, D.K. Rao, Effect of Bi_2O_3 proportion on physical, structural and electrical properties of zinc bismuth phosphate glasses. *J. non-crys. sol.* **357**(21), 3585–3591 (2011)
 49. N. Vedeanu, O. Cozar, R. Stanescu, I.B. Cozar, I. Ardelean, Structural investigation of new vanadium–bismuth–phosphate glasses by IR and ESR spectroscopy. *J. Mol. Str.* **1044**, 323–327 (2013)
 50. N. Kitamura, K. Fukumi, J. Nakamura, T. Hidaka, T. Ikeda, H. Hashima, J. Nishii, Optical properties of fluorine-substituted zinc bismuth phosphate glasses. *J. Non-Crys. Sol.* **357**(3), 1188–1192 (2011)
 51. B.A. Sava, L. Boroica, M. Elisa, O. Shikimaka, D. Grabco, M. Popa, R.C.C. Monteiro, Bismuth and lead oxides codoped boron phosphate glasses for Faraday rotators. *Cer. Inter.* **44**(6), 6016–6025 (2018)
 52. J. Jiráček, L. Koudelka, J. Pospíšil, P. Mošner, L. Montagne, L. Delevoye, Study of structure and properties of $\text{ZnO-Bi}_2\text{O}_3\text{-P}_2\text{O}_5$ glasses. *J. mat. sci.* **42**(20), 8592–8598 (2007)
 53. R.V.S.S.N. Ravikumar, V.R. Reddy, A.V. Chandrasekhar, B.J. Reddy, Y.P. Reddy, P.S. Rao, Tetragonal site of transition metal ions doped sodium phosphate glasses. *J; allo. and comp.* **337**(1–2), 272–276 (2002)
 54. L.D. Bogomolova, V.A. Jachkin, V.N. Lazukin, T.K. Pavlushkina, V.A. Shmuckler, The electron paramagnetic resonance and optical spectra of copper and vanadium in phosphate glasses. *J. Non-Cry. Sol.* **28**(3), 375–389 (1978)
 55. P. Kaur, K.J. Singh, S. Thakur, P. Singh, B.S. Bajwa, Investigation of bismuth borate glass system modified with barium for structural and gamma-ray shielding properties. *Spect. Acta. Mol. Bio. Spect.* **206**, 367–377 (2019)
 56. A. Kumar, D.K. Gaikwad, S.S. Obaid, H.O. Tekin, O. Agar, M.I. Sayyed, Experimental studies and Monte Carlo simulations on gamma ray shielding competence of $(30+x)\text{PbO}_{10}\text{-WO}_3\text{-10Na}_2\text{O-10MgO-(40-x)}\text{B}_2\text{O}_3$ glasses. *Prog. Nucl. Ener.* **119**, 103047 (2020)
 57. Y. Al-Hadeethi, M.I. Sayyed, $\text{BaO-Li}_2\text{O-B}_2\text{O}_3$ glass systems: potential utilization in gamma radiation protection. *Prog. Nucl. Ener.* **129**, 103511 (2020)
 58. S.A. Issa, M. Ahmad, H.O. Tekin, Y.B. Saddeek, M.I. Sayyed, Effect of Bi_2O_3 content on mechanical and nuclear radiation shielding properties of $\text{Bi}_2\text{O}_3\text{-MoO}_3\text{-B}_2\text{O}_3\text{-SiO}_2\text{-Na}_2\text{O-Fe}_2\text{O}_3$ glass system. *Results Phys* **13**, 102165 (2019)

Publisher's Note Springer Nature remains neutral with regard to jurisdictional claims in published maps and institutional affiliations.

Springer Nature or its licensor (e.g. a society or other partner) holds exclusive rights to this article under a publishing agreement with the author(s) or other rightsholder(s); author self-archiving of the accepted manuscript version of this article is solely governed by the terms of such publishing agreement and applicable law.